

FIG. 1. (a) Schematic of the lattice. A hexagonal inner domain (yellow) is surrounded by an outer domain (white). In the Hermitian and linear regime, the inner domain is a higher order topological insulator (HOTI) and the outer domain is trivial. In the close-up view (right panel), dashes mark out one unit cell, thin (thick) lines indicate intracell (intercell) couplings $t_1 = 1 - \delta$ ($t_2 = 1 + \delta$), sites with gain (loss) are filled red (unfilled blue) circles, and the reflection symmetry operations \mathcal{P} and \mathcal{P}' are indicated. (b) Linear spectrum, plotted against the gain/loss parameter γ for $\delta = 0.6$. Left panel: $\text{Re}[E]$ versus γ . At $\gamma = 0$, there are six mid-gap corner states, which undergo \mathcal{PT} breaking as $|\gamma|$ is increased. Right panel: zoomed-in plot of $\text{Re}[E]$ (solid curves) and $\text{Im}[E]$ (dashes) versus γ . The branches labelled I and II are one- and two-fold degenerate respectively. Square and star markers indicate the modes in Fig. 2. The number of non-real eigenvalues in each γ range is shown in parentheses.

states not even having the lowest threshold. The use of \mathcal{PT} breaking to stabilize non-topological single-mode lasing has previously been demonstrated [54, 55], and the present work shows that single-mode lasing based on topological HOTI corner states can be protected in a similar way, through the suppression of competing edge and bulk states. This points to further opportunities for using the combination of non-Hermitian effects and band topology, a subject of considerable recent theoretical interest [56], in the design of future topological laser devices.

Our analysis is performed using a tight-binding model containing nearest-neighbor couplings, with each site representing an optical resonator (a similar approach has been successfully used to model real PTI lasers [14, 17, 26, 27]). The model is both non-Hermitian and nonlinear: the pumped lattice sites are modelled with saturable gain dependent on the local site intensity, while the remaining lattice sites are subject to linear fixed loss (representing a combination of outcoupling loss and material absorption). The above-threshold behavior of the

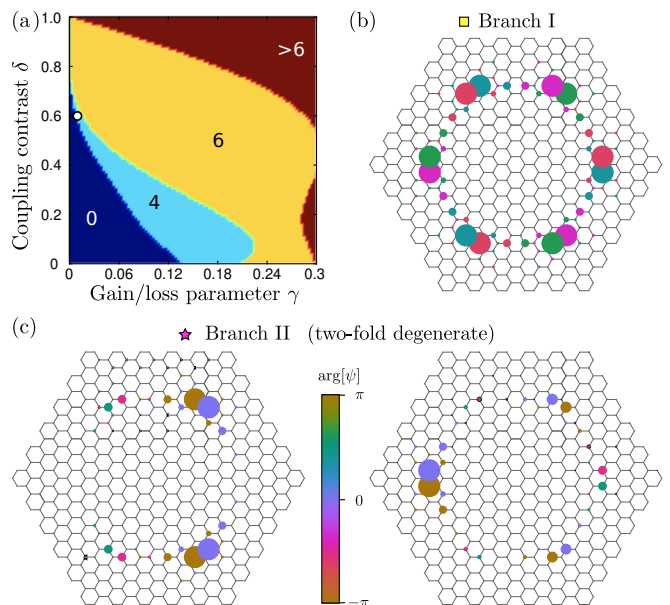


FIG. 2. (a) Phase diagram showing the number of \mathcal{PT} -broken eigenstates versus γ and δ . The white dot indicates a representative point with parameters $\gamma = 0.012$ and $\delta = 0.6$, used in other subplots. (b)–(c) Intensity and phase distribution of selected eigenstates, corresponding to the markers in Fig. 1(b). The area of the circles is proportional to the intensity, and the color indicates the phase. (b) Eigenstate on the non-degenerate branch I, which is \mathcal{PT} symmetric (real E) and antisymmetric under \mathcal{P}' . (c) Eigenstates on the degenerate branch II, which are \mathcal{PT} broken with $\text{Im}(E) > 0$ (their damped \mathcal{PT} partners are not shown), and \mathcal{P}' -symmetric (left) and \mathcal{P}' -antisymmetric (right) respectively.

laser is studied using both frequency-domain eigenmode analysis and time-domain simulations.

The model, depicted in Fig. 1(a), is a Wu-Hu lattice [57] with gain/loss added to alternate sites. There are six sites per unit cell, and the intracell (intercell) couplings are $t_1 = 1 - \delta$ ($t_2 = 1 + \delta$), where δ is a real tuning parameter. In a real system, such as a photonic crystal or waveguide array, δ may be set by the ratio of distances between inter- and intra-cell structural elements [43, 44, 57]. In the inner (outer) domain, $\delta > 0$ ($\delta < 0$). In the absence of gain/loss, the inner domain is a higher-order topological insulator (HOTI) in the nontrivial topological phase [46, 49], surrounded by a topologically trivial cladding, so topological corner states will occur at each of the six corners of the domain. Similar to previously-studied HOTI lasers [22–25], the higher-order topology is tied to the “filling anomaly” of the C_{6v} -symmetric topological crystalline insulator [46, 49]. Next, we subdivide the sites into two sublattices, A (gain) and B (loss), drawn as red and blue circles in the right panel of Fig. 1(a). In the

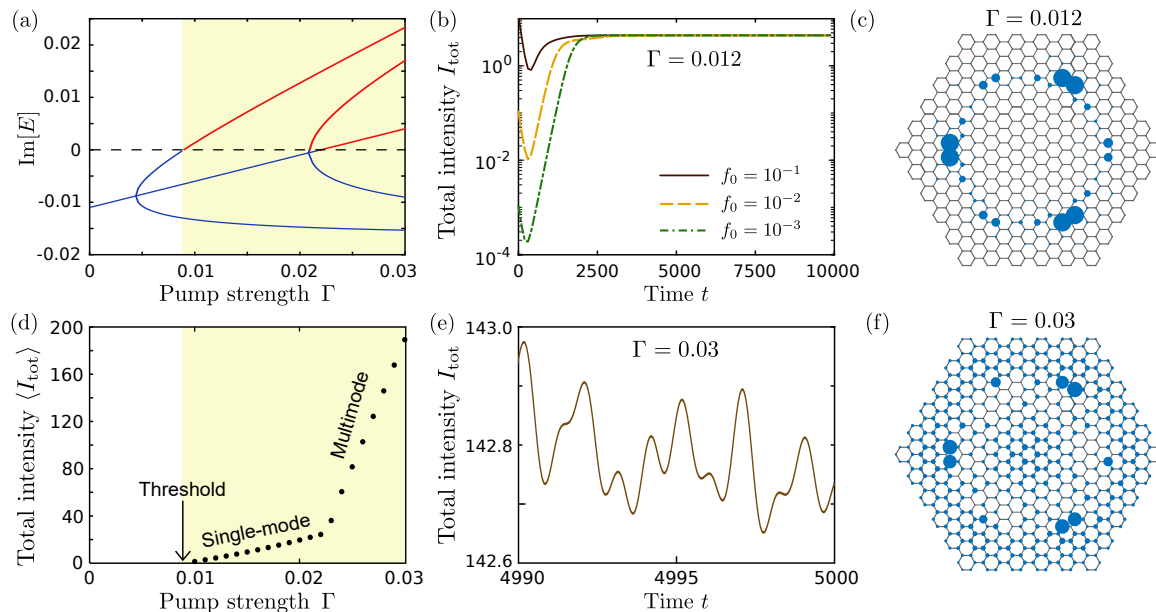


FIG. 3. (a) Plot of $\text{Im}[E]$ versus pump parameter Γ for the corner states, in the linear regime (no gain saturation). Lasing occurs upon crossing $\text{Im}[E] = 0$ (horizontal dashes); the above-threshold regime is marked in yellow. In this and subsequent subplots, we take $\gamma_0 = 0.005$, $\gamma_B = 0.017$, and $\delta = 0.6$. (b) Time dependence of the total intensity $I_{\text{tot}} = \sum_n |\psi_n|^2$, with $\Gamma = 0.012$ and gain saturation enabled. Each site is initialized to $(\alpha + i\beta)f_0$, where α and β are random numbers drawn from the standard normal distribution and the constant f_0 determines the magnitude of the initial excitation; results are shown for three independent initial conditions with different f_0 , showing convergence to the same steady state I_{tot} . (c) Intensity distribution in the steady state. A comparison with Fig. 2(c) shows that the lasing mode is a superposition of \mathcal{P}' -symmetric and \mathcal{P}' -antisymmetric modes with broken \mathcal{PT} . (d) Time-averaged total intensity $\langle I_{\text{tot}} \rangle$ versus Γ . The kink at $\Gamma \approx 0.022$ corresponds to the onset of multimode lasing. The $\langle I_{\text{tot}} \rangle$ values are obtained by averaging over $t \in [9000, 10000]$. (e) Time dependence of I_{tot} in the multimode regime, $\Gamma = 0.03$. For this t range, the transients have died away and the laser is in steady state. (f) Snapshot of intensity distribution in the multimode regime, taken at $t = 5000$ with the same parameters as in (e). In (c)–(f), the system is initialized with $f_0 = 0.01$, but the same results are obtained for other choices of f_0 .

position representation, the Hamiltonian is

$$H = \left\{ \sum_{r \in A} \sum_{i=1}^3 t_{r,s_i} a_r^\dagger b_{r+s_i} + \text{h.c.} \right\} + \sum_{r \in A} i\gamma_A(r) a_r^\dagger a_r - \sum_{r \in B} i\gamma_B b_r^\dagger b_r, \quad (1)$$

where a_r (b_r) denotes the annihilation operator on the A (B) site at position r ; $s_{1,2,3}$ are nearest neighbor displacement vectors; $t_{r,s_i} \in [t_1, t_2]$ are nearest neighbor hoppings assigned as stated above; $\gamma_A(r)$ is a gain term on each A site, to be discussed below; and γ_B is a loss term for the B sites. Each eigenvalue of H , denoted by E , represents a detuning relative to a principal frequency.

We first analyze the system in the absence of gain saturation and with balanced gain/loss $\gamma_A = \gamma_B = \gamma$. The lattice is \mathcal{PT} symmetric [53], where \mathcal{P} is a reflection around the vertical axis as indicated in Fig. 1(a), and \mathcal{T} is complex conjugation. Fig. 1(b) plots the eigenvalue spectrum versus γ for $\delta = 0.6$. At $\gamma = 0$, there are six eigenstates in two sub-bands near $E = 0$, which are the six HOTI corner states; there is some hybridization-induced splitting due to the finite separation between

corners. As $|\gamma|$ is increased, the corner states successively undergo \mathcal{PT} breaking [50–53]: the eigenvalues coalesce at $\text{Re}[E] = 0$ and become imaginary, as shown in the right panel of Fig. 1(b). The two-fold degenerate branches labelled II break \mathcal{PT} first; the non-degenerate outer branches labelled I break \mathcal{PT} for larger $|\gamma|$.

Notably, the lattice's other eigenstates (i.e., bulk and edge states) have unbroken \mathcal{PT} symmetry over the entire range of γ shown here, and their eigenvalues are real. In other words, *the corner states undergo \mathcal{PT} breaking first*. In the lasing model to be discussed below, this is the key to producing laser modes from the topological corner states. For much larger $|\gamma|$, the other eigenstates eventually break \mathcal{PT} and acquire complex eigenvalues. Fig. 2(a) shows the phase diagram for the number of non-real eigenvalues versus γ and δ . The \mathcal{PT} breaking of the corner states depends not only on γ , but also on the effective coupling between the corners, which is determined by both δ and the system size. In the infinite lattice limit where the corners do not couple, the \mathcal{PT} -breaking transition is thresholdless [58, 59].

Aside from \mathcal{PT} symmetry, the lattice is invariant under reflection across the horizontal axis, denoted by \mathcal{P}' . The non-degenerate branch I is antisymmetric under \mathcal{P}' ,

and the two-fold degenerate branch II contains a \mathcal{P}' -symmetric and a \mathcal{P}' -antisymmetric mode. The \mathcal{P}' symmetry/antisymmetry persists through the \mathcal{PT} breaking transition. Fig. 2(b)–(c) shows three exemplary mode profiles at $\gamma = 0.012$ and $\delta = 0.6$, for which branch I is \mathcal{PT} symmetric and branch II is \mathcal{PT} broken.

We now develop the tight-binding model into a laser model by introducing gain saturation according to

$$\gamma_A = \frac{\Gamma}{1 + |\psi_n|^2} - \gamma_0. \quad (2)$$

This describes a combination of saturable gain and background loss, where Γ parameterizes the pump strength (taken to be the same on all A sites), $|\psi_n|^2$ is the intensity on site n , and γ_0 is a background loss. Each B site is assigned a fixed loss γ_B . The losses are due to some combination of outcoupling loss and material absorption, such that the laser's output power can be assumed to be proportional to the total intensity $I_{\text{tot}} = \sum_n |\psi_n|^2$.

For $|\psi_n|^2 \rightarrow 0$, this is a linear lattice with \mathcal{PT} symmetric gain/loss $\gamma = (\Gamma - \gamma_0 + \gamma_B)/2$ plus additional loss $\gamma' = (\gamma_B + \gamma_0 - \Gamma)/2$ on all sites. Fig. 3(a) shows the plot of $\text{Im}[E]$ versus Γ for the corner states. With increasing Γ , the corner states undergo bifurcations [52] that map to the previously-discussed \mathcal{PT} breaking transitions. Note that these are unrelated to the bifurcations of nonlinear dynamical systems. The bulk and edge modes map to \mathcal{PT} unbroken modes and have damping rate $\text{Im}[E] = -\gamma'$. The laser threshold occurs when one branch of corner states reaches $\text{Im}[E] = 0$.

Above threshold, the gain saturation in Eq. (2) must be accounted for. Fig. 3(b) shows time-domain simulations for the total intensity I_{tot} at pump strength $\Gamma = 0.012$. The initial complex amplitude on each site n is set to $\psi_n(t=0) = (\alpha_n + i\beta_n)f_0$, where α_n and β_n are drawn independently from the standard normal distribution and f_0 is an overall scale factor for the initial state. The three curves in Fig. 3(b) corresponding to different f_0 all converge to the same I_{tot} at large times, indicating that the system operates as a stable single-mode laser. Fig. 3(c) shows the steady state intensity profile. Comparing this to Fig. 2, we see that the laser mode is a superposition of the \mathcal{P}' -symmetric and \mathcal{P}' -antisymmetric modes of branch II. We verified numerically that the steady-state field distribution is indeed an equal-amplitude linear superposition of the two corner states in Fig. 2(c).

Fig. 3(d) shows the input-output curve (i.e., time-averaged total intensity versus pump strength Γ), obtained by time domain simulations. The laser is single-mode up to about 2.4 times threshold ($\Gamma \approx 0.022$); the subsequent kink in the curve corresponding to the onset of multimode lasing. For these calculations, we take $f_0 = 0.01$ for the initial conditions and average I_{tot} over a time window $t \in [9000, 10000]$ (after transient oscillations have died away); we also verified that the resulting intensity curve is independent of f_0 . Fig. 3(e) shows the complicated oscillations of I_{tot} in this regime. Fig. 3(f) shows the intensity profile at a typical instant, confirm-

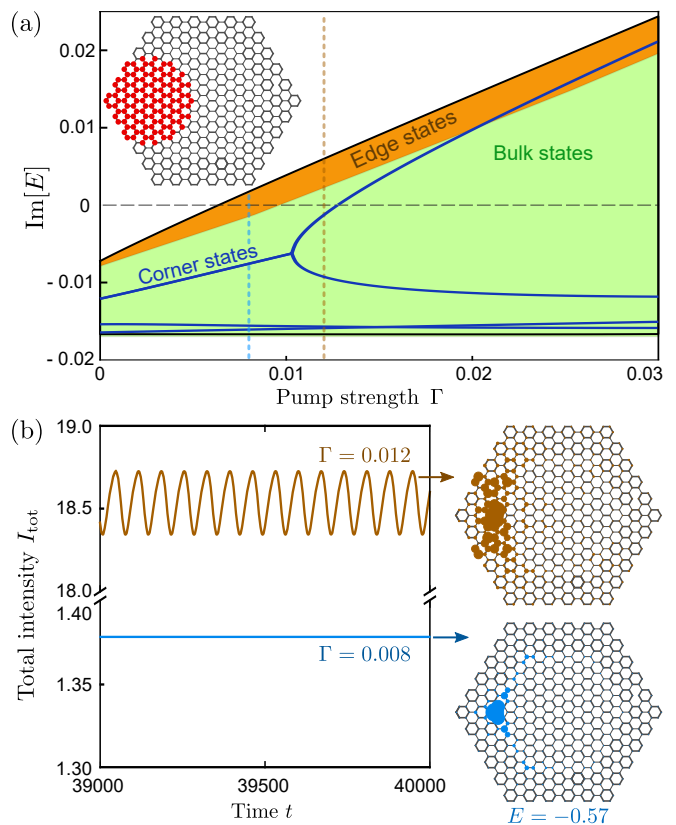


FIG. 4. (a) Plot of $\text{Im}[E]$ versus pump parameter Γ for all eigenstates of a selectively pumped lattice, in the linear regime with no gain saturation. The corner states are denoted by solid lines, and the areas marked in orange and green indicate where the edge and bulk states reside (the numerous individual edge and bulk states are not plotted for clarity). Inset: schematic of the lattice with pumped sites marked by red circles. The other sites all have loss $\gamma_A = \gamma_B = 0.017$. In this and subsequent subplots, we take $\gamma_0 = 0.005$ and $\delta = 0.6$. (b) Time dependence of the total intensity $I_{\text{tot}} = \sum_n |\psi_n|^2$ for $\Gamma = 0.008$ (blue curve) and $\Gamma = 0.012$ (brown curve) with gain saturation enabled. Each site is initialized to $(\alpha + i\beta)f_0$, where α, β are drawn from the standard normal distribution and $f_0 = 0.01$. The right panels show snapshots of the intensity distributions taken at $t = 40000$.

ing that the extra laser modes arise from bulk states; although the corner modes are visible, most of the output power is emitted from the more numerous bulk sites. The threshold and dynamic range of the single-mode lasing regime depends on δ and the system size, as discussed in the Supplemental Materials [58].

To demonstrate the qualitative difference between the \mathcal{PT} -stabilized HOTI laser and a more standard design, Fig. 4 shows the performance of a HOTI laser with a spatially selective pump. The passive part of the HOTI lattice is the same as before, but all the sites near one domain corner are pumped, as illustrated in the inset of Fig. 4(a). The plot of $\text{Im}(E)$ versus pump strength Γ , in the absence of gain saturation, is shown in Fig. 4(a). We see that the edge states and bulk states acquire

effective gain comparable to and in some cases higher than the topological corner states. Fig. 4(b) shows the time-dependent total intensity for two values of Γ ; at $\Gamma = 0.008$, prior to the topological corner states reaching threshold, a mode evolving out of the edge state bands has already lased, as shown in the lower right panel of Fig. 4(b). The mode frequency, determined via Fourier transformation, is $E = -0.57$, outside the band of topological corner states. At a slightly larger pump, $\Gamma = 0.012$, the lasing is multimode. Further time domain simulations reveal that single-mode lasing occurs over a relatively narrower range of pump strengths, as shown in the Supplemental Materials [58]. While this paper was in review, we noticed another paper concerning \mathcal{PT} -symmetry in a similar lattice [60], which focused on the \mathcal{PT} -breaking of the Bloch states rather than the topological corner states considered in this work.

We have thus demonstrated that by applying \mathcal{PT} symmetric gain and loss to a HOTI lattice, topological corner states can be made to lase preferentially in a single mode

over a wide dynamic range. Competing edge and bulk states have significantly higher thresholds, in spite of spatial hole burning (local gain saturation), and without a frequency-selective gain medium. The higher gain experienced by the topological laser mode arises from \mathcal{PT} symmetry breaking, which has previously been shown to stabilize non-topological laser modes [50–53]. Such a laser can be implemented with a 2D photonic crystal, as shown in the Supplemental Materials [58]. In future work, it would be interesting to study how other non-Hermitian symmetry breakings, and other inherently non-Hermitian phenomena, could be usefully incorporated into topological lasers.

This work was supported by the Singapore MOE Academic Research Fund Tier 3 Grant MOE2016-T3-1-006, Tier 2 Grant MOE2018-T2-1-176, Tier 2 Grant MOE2016-T2-2-159, Tier 2 Grant MOE2019-T2-2-085, Tier 1 Grants RG187/18, and Singapore National Research Foundation (NRF) Competitive Research Program (CRP) (NRF-CRP18-2017-02).

-
- [1] L. Lu, J. Joannopoulos and M. Soljačić, Topological photonics, *Nat. Photonics* **8**, 821 (2014).
- [2] T. Ozawa, H. Price, A. Amo, N. Goldman, M. Hafezi, L. Lu, M. Rechtsman, D. Schuster, J. Simon, O. Zeitlinger and I. Carusotto, Topological photonics, *Rev. Mod. Phys.* **91**, 015006 (2019).
- [3] F. Haldane and S. Raghu, Possible Realization of Directional Optical Waveguides in Photonic Crystals with Broken Time-Reversal Symmetry, *Phys. Rev. Lett.* **100**, 013904 (2008).
- [4] S. Raghu and F. Haldane, Analogs of quantum-Hall-effect edge states in photonic crystals, *Phys. Rev. A* **78**, 033834 (2008).
- [5] Z. Wang, Y. Chong, J. Joannopoulos and M. Soljačić, Observation of unidirectional backscattering-immune topological electromagnetic states, *Nature* **461**, 772 (2009).
- [6] M. Hafezi, E. A. Demler, M. D. Lukin, and J. M. Taylor, Robust optical delay lines with topological protection, *Nat. Phys.* **7**, 907 (2011).
- [7] M. Hafezi, S. Mittal, J. Fan, A. Migdall, and J. M. Taylor, Imaging topological edge states in silicon photonics, *Nat. Photon.* **7**, 1001 (2013).
- [8] S. Barik, A. Karasahin, C. Flower, T. Cai, H. Miyake, W. DeGottardi, M. Hafezi and E. Waks, A topological quantum optics interface, *Science* **359**, 666 (2018).
- [9] Y. Yang, Y. Yamagami, X. Yu, P. Pitchappa, J. Webber, B. Zhang, M. Fujita, T. Nagatsuma and R. Singh, Terahertz topological photonics for on-chip communication, *Nat. Photon.* **14**, 446 (2020).
- [10] V. Peano, M. Houde, F. Marquardt, and A. A. Clerk, Topological Quantum Fluctuations and Traveling Wave Amplifiers, *Phys. Rev. X* **6**, 041026 (2016).
- [11] D. Smirnova, S. Kruk, D. Leykam, E. Melik-Gaykazyan, D.-Y. Choi, and Y. Kivshar, Third-Harmonic Generation in Photonic Topological Metasurfaces, *Phys. Rev. Lett.* **123**, 103901 (2019).
- [12] P. St-Jean, V. Goblot, E. Galopin, A. Lemaitre, T. Ozawa, L. Le Gratiet, I. Sagnes, J. Bloch, and A. Amo, Lasing in topological edge states of a one-dimensional lattice, *Nat. Photon.* **11**, 651 (2017).
- [13] S. Longhi, Non-Hermitian gauged topological laser arrays, *Ann. Phys. (Berl.)* **530**, 1800023 (2018).
- [14] H. Zhao, P. Miao, M. H. Teimourpour, S. Malzard, R. E. Ganainy, H. Schomerus and L. Feng, Topological hybrid silicon microlasers, *Nat. Commun.* **9**, 981 (2018).
- [15] M. Parto, S. Wittek, H. Hodaei, G. Harari, M. A. Bandres, J. Ren, M. C. Rechtsman, M. Segev, D. N. Christodoulides, and M. Khajavikhan, Edge-Mode Lasing in 1D Topological Active Arrays, *Phys. Rev. Lett.* **120**, 113901 (2018).
- [16] Y. Ota, R. Katsumi, K. Watanabe, S. Iwamoto and Y. Arakawa, Topological photonic crystal nanocavity laser, *Commun. Phys.* **1**, 86 (2018)
- [17] G. Harari, Miguel. A. Bandres, Y. Lumer, M. C. Rechtsman, Y. D. Chong, M. Khajavikhan, D. N. Christodoulides, M. Segev, Topological insulator laser: theory, *Science* **359**, 6381 (2018).
- [18] M. A. Bandres, S. Steffen, G. Harari, M. Parto, J. Ren, M. Segev, D. N. Christodoulides, M. Khajavikhan Topological insulator laser: Experiments, *Science* **359**, 6381 (2018).
- [19] Y. Zeng, U. Chattopadhyay, B. Zhu, B. Qiang, J. Li, Y. Jin, L. Li, A. G. Davies, E. H. Linfield, B. Zhang, Y. D. Chong and Q. J. Wang, Electrically pumped topological laser with valley edge modes, *Nature* **578**, 246 (2020).
- [20] X. Gao, L. Yang, H. Lin, L. Zhang, J. Li, F. Bo, Z. Wang and L. Lu, Dirac-vortex topological cavities, *Nat. Nanotechnol.* **15**, 1012 (2020).
- [21] Z. Yang, E. Lustig, G. Harari, Y. Plotnik, Y. Lumer, M. A. Bandres and M. Segev, Mode-Locked Topological Insulator Laser Utilizing Synthetic Dimensions, *Phys. Rev. X* **10**, 011059 (2020)
- [22] H. Kim, M. Hwang, D. Smirnova, K. Jeong, Y. Kivshar and H. Park, Multipolar lasing modes from topological

- corner states, *Nat. Commun.* **11**, 5758 (2020).
- [23] W. Zhang, X. Xie, H. Hao, J. Dang, S. Xiao, S. Shi, H. Ni, Z. Niu, C. Wang, K. Jin, X. Zhang and X. Xu, Low-threshold topological nanolasers based on the second-order corner state, *Light Sci. Appl.* **9**, 109 (2020).
- [24] C. Han, M. Kang and H. Jeon, Lasing at Multidimensional Topological States in a Two-Dimensional Photonic Crystal Structure, *ACS Photonics* **7**, 2027 (2020).
- [25] H. Zhong, Y. Kartashov, A. Szameit, Y. Li, C. Liu and Y. Zhang, Theory of topological corner state laser in Kagome waveguide arrays, *APL Photonics* **6**, 040802-1 (2021).
- [26] D. Smirnova, A. Tripathi, S. Kruk, M. Hwang, H. Kim, H. Park and Y. Kivshar, Room-temperature lasing from nanophotonic topological cavities, *Light. Sci. Appl.* **9**, 127 (2020).
- [27] Z. Shao, H. Chen, S. Wang, X. Mao, Z. Yang, S. Wang, X. Wang, X. Hu and R. Ma, A high-performance topological bulk laser based on band-inversion-induced reflection, *Nat. Nanotechnol.* **15**, 67, (2020)
- [28] W. Noh, H. Nasari, H. Kim, Q. Van, Z. Jia, C. Huang and B. Kanté, Experimental demonstration of single-mode topological valley-Hall lasing at telecommunication wavelength controlled by the degree of asymmetry, *Opt. Lett.* **45**, 4108 (2020).
- [29] D. Smirnova, D. Leykam, Y. D. Chong and Y. Kivshar, Nonlinear topological photonics, *Appl. Phys. Rev.* **7**, 021306 (2020).
- [30] Y. Ota, K. Takata, T. Ozawa, A. Amo, Z. Jia, B. Kante, M. Notomi, Y. Arakawa and S. Iwamoto, Active topological photonics, *Nanophotonics* **9**, 547 (2020).
- [31] S. Malzard and H. Schomerus, Nonlinear mode competition and symmetry-protected power oscillations in topological lasers, *New J. Phys.* **20**, 063044 (2018).
- [32] S. Longhi, Y. Kominis, and V. Kovanis, Presence of temporal dynamical instabilities in topological insulator lasers, *Europhys. Lett.* **122**, 14004 (2018).
- [33] Y. V. Kartashov and D. V. Skryabin, Two-Dimensional Topological Polariton Laser, *Phys. Rev. Lett.* **122**, 083902 (2019).
- [34] M. Seclì, M. Capone and I. Carusotto, Theory of chiral edge state lasing in a two-dimensional topological system, *Phys. Rev. Res.* **1**, 033148 (2019).
- [35] M. Seclì, T. Ozawa, M. Capone, and I. Carusotto, Spatial and Spectral Mode-Selection Effects in Topological Lasers with Frequency-Dependent Gain, *APL Photonics* **6**, 050803 (2021).
- [36] I. Amelio and I. Carusotto, Theory of the Coherence of Topological Lasers, *Phys. Rev. X* **10**, 041060 (2020).
- [37] P. Zapletal, B. Galilo and A. Nunnenkamp, Long-lived elementary excitations and light coherence in topological lasers, *Optica* **7**, 1045 (2020).
- [38] S. Gündoğdu, J. Thingna and D. Leykam, Edge mode bifurcations of two-dimensional topological lasers, *Opt. Lett.* **45**, 3673 (2020).
- [39] A. Dikopoltsev, T. H. Harder, E. Lustig, O. A. Egorov, J. Beierlein, A. Wolf, Y. Lumer, M. Emmerling, C. Schneider, S. Höfling, M. Segev and S. Klembt, Topological insulator vertical-cavity laser array, *Science* **373**, 1514 (2021).
- [40] M. Parto, Y. Liu, B. Bahari, M. Khajavikhan and D. Christodoulides, Non-Hermitian and topological photonics: optics at an exceptional point, *Nanophotonics* **10**, 403 (2021).
- [41] W. A. Benalcazar, B. A. Bernevig, and T. L. Hughes, Quantized electric multipole insulators, *Science* **357**, 61 (2017).
- [42] F. Schindler, A. M. Cook, M. G. Vergniory, Z. J. Wang, S. S. P. Parkin, B. A. Bernevig, and T. Neupert, Higher-order topological insulators, *Sci. Adv.* **4**, eaat0346 (2018).
- [43] M. Serra-Garcia, V. Peri, R. Süsstrunk, O. Bilal, T. Larsen, L. Villanueva and S. Huber, Observation of a phononic quadrupole topological insulator, *Nature* **555**, 342 (2018).
- [44] S. Mittal, V. Orre, G. Zhu, M. Gorkach, A. Poddubny and M. Hafezi, Photonic quadrupole topological phases, *Nat. Photonics* **13**, 692 (2019).
- [45] X. Zhou, Z. Lin, W. Lu, Y. Lai, B. Hou and J. Jiang, Twisted quadrupole topological photonic crystals, *Laser Photonics Rev.* **14**, 2000010, 2020.
- [46] W. A. Benalcazar, T. H. Li and T. L. Hughes, Quantization of fractional corner charge in C_n -symmetric higher-order topological crystalline insulators, *Phys. Rev. B* **99**, 245151 (2019).
- [47] X. Chen, W. Deng, F. Shi, F. Zhao, M. Chen and J. Dong, Direct observation of corner states in second-order topological photonic crystal slabs, *Phys. Rev. Lett.* **122**, 233902 (2019).
- [48] A. Hassan, F. Kunst, A. Moritz, G. Andler, E. Bergholtz and M. Bourennane, Corner states of light in photonic waveguides, *Nat. Photonics* **13**, 697 (2019).
- [49] B. Y. Xie, G. X. Su, H. F. Wang, F. Liu, L. M. Hu, S. Y. Yu, P. Zhan, M. H. Lu, Z. L. Wang and Y. F. Chen, Higher-order quantum spin Hall effect in a photonic crystal, *Nat. Commun.* **11**, 3768 (2020).
- [50] H. Schomerus, Topologically protected midgap states in complex photonic lattices, *Opt. Lett.* **38**, 1912 (2013).
- [51] S. Longhi, Parity-time symmetry meets photonics: A new twist in non-Hermitian optics, *EPL (Europhysics Letters)* **120**, 64001 (2017).
- [52] L. Feng, R. El-Ganainy and L. Ge, Non-Hermitian photonics based on parity-time symmetry, *Nat. Photon.* **11**, 752 (2017).
- [53] R. El-Ganainy, K. G. Makris, M. Konstantinos, Z. H. Musslimani, S. Rotter and D. N. Christodoulides, Non-Hermitian physics and PT symmetry, *Nat. Phys.* **14**, 11 (2018).
- [54] L. Feng, Z. J. Wong, R. M. Ma, Y. Wang, X. Zhang, Single-mode laser by parity-time symmetry breaking, *Science* **346**, 972 (2014).
- [55] H. Hodaei, M. A. Miri, M. Heinrich, D. N. Christodoulides and M. Khajavikhan, Parity-time-symmetric microring lasers, *Science* **346**, 975 (2014).
- [56] E. J. Bergholtz, J. C. Budich, and F. K. Kunst, Exceptional topology of non-Hermitian systems, *Rev. Mod. Phys.* **93**, 015005 (2021).
- [57] L. H. Wu and X. Hu, Scheme for Achieving a Topological Photonic Crystal by Using Dielectric Material, *Phys. Rev. Lett.* **114**, 223901 (2015).
- [58] See online Supplementary Material.
- [59] L. Ge and A. D. Stone, Parity-Time Symmetry Breaking beyond One Dimension: The Role of Degeneracy, *Phys. Rev. X* **4**, 031011 (2014).
- [60] M. L. N. Chen, L. J. Jiang, S. Zhang, R. Zhao, Z. Lan and W. E. I. Sha, Comparative study of Hermitian and non-Hermitian topological dielectric photonic crystals, *Phys. Rev. A* **104**, 033501 (2021).